International Journal of Nanomedicine

Dovepress
Taylor & Francis Group

Open Access Full Text Article

ORIGINAL RESEARCH

Bioinspired RGD-Functionalized Gold Nanoparticles for Integrin-Driven Interaction with Melanoma Cells

Annarita Del Gatto[1,2,*], Patrizia Di Pietro[3,*], Michele Saviano[2,4], Marianna Flora Tomasello[4], Giuseppe Pappalardo[4], Rony Snyders[5,6], Giuseppe Forte[7], Cristina Satriano[3], Laura Zaccaro[1,2]

[1]Institute of Biostructures and Bioimaging (IBB), Naples, Italy; [2]Interuniversity Research Centre on Bioactive Peptides (CIRPeB) "carlo Pedone", University of Naples, Naples, Italy; [3]NanoHybrid Biointerfaces Laboratory (NHBIL), Department of Chemical Sciences, University of Catania, Catania, Italy; [4]Institute of Crystallography (IC), Bari, Italy; [5]Plasma-Surface Interaction Chemistry, University of Mons, Mons, Belgium; [6]Materia Nova Research Center, Mons, Belgium; [7]Department of Drug and Health Sciences, University of Catania, Catania, Italy

*These authors contributed equally to this work

Correspondence: Cristina Satriano, Department of Chemical Sciences, University of Catania, Viale Andrea Doria, 6, Catania, 95125, Italy, Tel +39 0957385136, Email cristina.satriano@unict.it

Purpose: In this study, we investigated the physicochemical properties, biofunctionalization and internalization mechanisms of peptide-functionalized gold nanoparticles (GNPs), with a particular focus on a cyclic $a_v\beta_3$ integrin-targeting ligand (cRGD), embedded in a scaffold comprising a gold-binding glycine-cysteine tetrapeptide (GCt) and a fluorescein isothiocyanate (FITC) dye.

Methods: The characterisation of the GNPs and their biofunctionalised counterparts (b-GNPs) was carried out by a series of techniques including dynamic light scattering (DLS), zeta potential (ζ) measurements, UV-visible (UV-vis) spectroscopy, scanning electron microscopy (SEM), Fourier transform infrared spectroscopy (FTIR), X-ray photoelectron spectroscopy (XPS) and theoretical modelling. Cellular uptake experiments were performed in human adenocarcinoma (HeLa, $a_v\beta_3$ non-expressing cells, negative control) and metastatic melanoma (WM266, $a_v\beta_3$-overexpressing cells, positive control) cells to assess receptor-mediated internalization.

Results: The physicochemical characterisation confirmed the successful functionalisation of GNPs with the bioinspired multifunctional cRGD-GCt-FITC moiety. Detailed analysis of the nano-bio interface revealed distinct chemical states and evidence of charge transfer effects between the GNPs surface and the RGD-containing peptide. Cellular studies demonstrated selective uptake and preferential accumulation of b-GNPs in $a_v\beta_3$-overexpressing cells, with RGD-functionalised GNPs inducing notable pro-apoptotic effects.

Conclusion: This work provides new understanding of biomimetic gold nanoparticles and highlights their potential in tumour selective strategies, particularly for integring-targeted theranostics, while addressing toxicity and targeting limitations of current RGD- and gold nanoparticle-based nanomedicine.

Keywords: plasmonic nanoparticles, theranostics, targeting, cancer nanomedicine, peptide

Introduction

Gold nanoparticles (GNPs) have opened up a new frontier in medicine,[1–3] owing to their remarkable properties, including low toxicity, high biocompatibility, size tunability, ease of functionalisation, localized surface plasmon resonance (LSPR), and intrinsic anti-angiogenic and anti-metastatic therapeutic properties.[4,5] These features make GNPs highly suitable for both diagnostic imaging and therapeutic applications, a combination often termed "theranostics".[4,6–10]

The functionalization of GNPs enhances their properties and enables the development of nanoformulations with improved selectivity, targeting, cellular uptake and specificity,[11] while overcoming common drug delivery challenges such as poor solubility, low bioavailability and instability in biological environments. A particularly promising strategy is the use of bioinspired ligands, such as extracellular matrix (ECM) components, peptides or proteins, to modify the

Received: 10 March 2025
Accepted: 7 July 2025
Published: 3 October 2025

surface of GNPs.[12,13] This allows the nanoparticles to acquire selectivity and specificity for particular cell types. For example, specific peptide sequences can be used to control the behaviour of nanoparticles, including stabilising them against colloidal aggregation and directing them into desired cellular uptake pathways.[4,5]

Peptides such as the cyclic arginine-glycine-aspartate (cRGD) sequence have attracted particular attention for their ability to specifically bind integrins, including $\alpha_v\beta_3$, which are highly expressed on the surface of many tumour cells, including those in melanoma,[14] glioblastoma[15] and ovarian[16] cancer. This selective binding can enhance the delivery of therapeutic agents and improve targeting specificity.

Integrins, which are well-known cell adhesion receptors for ECM proteins, immunoglobulins, growth factors, cytokines and matrix-degrading proteases, play important roles in inflammation and cancer. Among the various integrins involved in angiogenesis, $\alpha_v\beta_3$ is particularly significant due to its involvement in the regulation of blood vessel formation[17–19] and its association with tumour and metastasis.[20]

There is a growing trend in biomedicine to integrate the RGD peptides with GNPs, with several examples in the literature describing both single[21–24] and multi-step[25–29] syntheses of linear and cyclic RGD-conjugated GNPs.[30,31] Although several decades have passed since the first preclinical studies with gold nanoconstructs, the transition from bench to bedside is still ongoing, with clinical trials progressing slowly.[32] A key consideration in this process is the length of the linker or spacer used to bioconjugate RGD peptides to GNPs. Often, RGD-conjugated GNPs contain polyethene glycol (PEG) moieties of varying lengths on their surface, either as spacers or alongside RGD peptides to prevent gold nanoparticle aggregation.[23,25,26,28] Recent studies suggest that PEGylation may present some issues, such as interference with the primary function of human erythrocytes,[33] immunotoxicity, clearance problems,[34] and apoptosis.[35] Another important consideration is the need to better understand the actual nano-bio interface between the RGDs and the GNPs.

A key aspect of this interaction is that RGDs bind to integrins on the cell surface, mediating cell adhesion and influencing cellular responses. When coupled to GNPs, this interaction could potentially enhance cellular uptake or improve targeting specificity. However, the exact way in which RGDs modify the properties of GNPs - whether through structural changes, alterations in surface charge, or other mechanisms - is not always fully understood.

Most studies primarily focus on validating the cellular uptake mechanism to confirm that the RGD peptides retain their ability to specifically target tumour cells after being immobilised on GNPs. Despite the extensive research on RGD-functionalised GNPs, there remains a limited understanding of the nano-bio interface between these nanoparticles and the peptides, which could further optimise their targeting and therapeutic potential.

In this study, we investigated biofunctionalized GNPs (b-GNPs), built via a combination of physisorption and chemisorption onto GNPs of the chimeric fluorescent peptide cRGD-GCt-FITC.[22,36,37] This multifunctional peptide combines a cyclic RGD sequence for integrin targeting, a gold binding glycine-cysteine tetrapeptide (GCt) for nanoparticle stabilization[38,39] and a fluorescein isothiocyanate (FITC) dye for imaging (Figure 1). Furthermore, due to its peptide-based nature, it may provide a bioinspired alternative to address the toxicity issues associated with PEG. Our focus was to investigate the physicochemical properties of these GNPs and their interactions with human adenocarcinoma (HeLa) cells ($\alpha v\beta_3$-negative) and metastatic melanoma (WM266) cells ($\alpha_v\beta_3$-overexpressing). Our aim was to evaluate the biofunctionalisation of these nanoparticles and their cellular uptake, to elucidate their potential as therapeutic agents themselves for theranostic applications in cancer therapy.

Materials and Methods

Synthetic Procedures and Experimental Characterisation

GNPs Fabrication

Chemicals were purchased from Sigma-Aldrich and used as received. Ultrapure MilliQ water (18.2 MΩ cm at 25 °C, Millipore) was employed. Glassware was cleaned prior to use by soaking in aqua regia ($HCl:HNO_3$, 1:3 volume ratio) and thoroughly rinsing with water. The buffer solution was prepared by dissolving 10 mM 3-(N-morpholino) propanesulfonic acid (MOPS), to which 2.7 mM KCl and 0.137 M NaCl were added. The reducing agent tris(2-carboxyethyl)

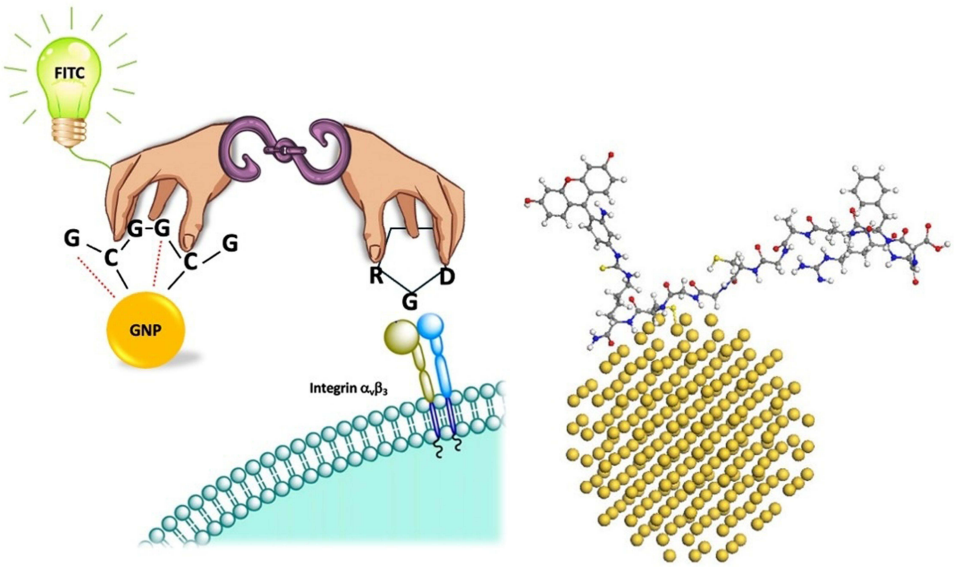

Figure 1 Graphical and constructed illustrations of the hybrid platform comprising b-GNPs, made of gold nanoparticles biofunctionalized with cRGD-GCt-FITC on their surface, designed for targeted interaction with the cell membrane.

phosphine (TCEP) was added to the MOPS solution at a 1:1 molar ratio, and the final pH was adjusted to 7.4 (25°C) with NaOH.

Preparation of Peptide-Functionalised GNPs

The peptide sequences FITC-$(GC)_2$ (MW=1081.32) and FITC-RGD $(GC)_2$ (MW=1625.55) were synthesised via Fmoc chemistry following a previously reported protocol.[37] Stock solutions of the peptides were prepared by dissolving 0.5 mg of lyophilised peptide powder in MOPS-TCEP buffer solution and stored at −20°C. Gold nanoparticles were synthesised by chemically reducing chloroauric acid with trisodium citrate. Briefly, gold (III) chloride hydrate ($HAuCl_4 \cdot xH_2O$) was dissolved in 20 mL of water in a beaker on a stirring hotplate to achieve a final concentration of 1 mM. 2 mL of a 1% solution of trisodium citrate dihydrate ($Na_3C_6H_5O_7 \cdot 2H_2O$) was then rapidly added to the vigorously stirred boiling solution. The gold sol gradually formed as citrate reduced the gold (III) ions. When the solution turned deep red, the beaker was removed from the heat and left to cool for about 10 minutes. This preparation resulted in particles of approximately 12 nm in diameter, with a plasmonic peak at 518 nm. The concentration of the synthesized gold nanoparticles was estimated to be 20 nM, with an extinction coefficient (ε) of 1.9×10^8 $M^{-1}cm^{-1}$, calculated using the equation: $\varepsilon = k \cdot \ln D + a$, where D is the core diameter of the nanoparticles, and k = 3.32111 and a = 10.80505 are constant.[40] The GNP@RGD hybrids were prepared by adding a 10 μM peptide solution to 1 mL of 20 nM GNP dispersion, followed by stirring and centrifugation (8000 rpm, 15 min at 25 °C). The resulting pellets were then dissolved in MilliQ water.

UV-Visible (UV-Vis) Spectroscopy

To investigate the plasmonic properties of the GNPs, electronic spectra were collected using a Jasco UV-vis spectrometer with quartz cuvettes (1 cm optical path length). To determine the inflection point of the LSPR peak,[41] the first and second-order derivative spectra were calculated from the extinction spectrum and then smoothed by using Microcal Origin software.

Fourier-Transformed Infrared (FT-IR) Spectroscopy

For FT-IR analysis, solutions were drop-cast onto a silica wafer and dried under a gentle stream of nitrogen. Infrared spectra were collected in the range from 500 cm-1 to 4000 cm^{-1} with a resolution of 1 cm^{-1} on a Bruker IFS 66v/s system.

https://doi.org/10.2147/IJN.S527082

X-Ray Photoelectron Spectroscopy (XPS)

XPS measurements to assess the surface composition and oxidation state were conducted using a PHI 5000 VersaProbe instrument, employing a monochromatic Al Kα X-ray source (1486.6 eV). High-resolution spectra of Au 4f, C1s, O1s, N1s and S2p signals were recorded at a pass energy and analyser energy step of 23.5 eV and 0.2 eV respectively. Fitting was carried out using software provided by PHI, with Shirley background subtraction applied. The spectra were calibrated for carbon contamination at a binding energy of 284.6 eV. All BE values are reported with an uncertainty ± 0.2 eV.

Dynamic Light Scattering (DLS) and Zeta Potential (ζ)

Hydrodynamic particle size analysis (via DLS) and nanoparticle surface charge (based on measurement of the particle electrophoretic mobility to calculate ζ) were performed using a NanoPartica SZ-100 instrument, equipped with a 514 nm laser (Horiba-Scientific). Measurements were conducted at 25°C, with data collected from three sequential readings. A minimum of five measurements were taken, and the results were averaged for analysis.

Scanning Electron Microscopy (SEM)

SEM images were captured using a Hitachi SU8020, equipped with a field emission gun and operating at an acceleration voltage of 30 kV, along with a transmission electron detector. Samples were mounted on 300 mesh, carbon-coated copper grids of agar and imaged directly.

Density Functional Theory (DFT) Modelling

All calculations were performed using Gaussian 16 software within the framework of Density Functional Theory (DFT). The dispersion-corrected M06L[42] functional was applied, along with the 6–311G(2d,p) basis set for the peptide and FITC. For the gold nanoparticle, a semi-empirical PM6 level was used.[43,44]

Cellular Studies

Cell Maintenance and Treatment

The human adenocarcinoma cell line (HeLa) (ECACC) was cultured in DMEM supplemented with 10% foetal bovine serum (FBS), 2 mM glutamine, 100 U/mL penicillin and 100 mg/mL streptomycin (Euroclone, Italy). The human metastatic melanoma cell line (WM266), kindly provided by Dr Gentilcore (IRCCS-Fondazione Pascale, Naples, Italy), was grown in RPMI, at physiological pH (7.2–7.4), supplemented with heat-inactivated 10% FBS, 1% glutamine, 100 U/mL penicillin and 100 mg/mL streptomycin. Both cell lines were maintained in a humidified incubator with 5% CO_2 at 37°C.

Integrin Content Determination

The specific detection and quantification of $\alpha_v\beta_3$ integrins were achieved through indirect immunofluorescence of non-permeabilized HeLa and WM266 cells using a conjugated monoclonal Alexafluor488 antibody targeting αvβ3 (LM609 - Millipore). Quantitative analysis was performed by flow cytometry. Briefly, approximately 100,000 HeLa and WM266 cells were harvested, washed once with PBS and pelleted. The cell pellet was fixed by incubation with 200 µL of 2% formaldehyde for 1 hour at room temperature. Fixed cells were blocked with 4% BSA and stained by incubation with 14 µg/mL of $\alpha_v\beta_3$ antibody for 45 min at 4°C. The stained cells were then washed twice and analysed using a CyFlow® ML flow cytometer (Partec). Cells were excited with an air-cooled argon 488 nm laser, and the AlexaFluor488 signal was detected on the FL1 detector in log mode. Data for 100,000 cells per sample were acquired, gated, and analysed using FlowMax software (Partec).

Cellular Uptake Analysis and Competition Binding Assay

Cells were seeded into 35 mm glass-bottomed cell culture plates (Willco Wells). After 24 hours, the cells were incubated with GNP@RGD$(GC)_2$-FITC or GNP@$(GC)_2$-FITC at a final concentration of 1.6 nM in HBSS buffer for 30 minutes at 37°C. The incubation was performed in the presence of 100 nM Lysotracker red and/or 10 µM Hoechst 33342 (Molecular Probes). Cells were then rinsed twice with PBS to remove excess peptide and imaged using a 63X oil immersion objective under a Leica DMI 6000B epifluorescence inverted microscope with adaptive focus control. This

system is equipped with a controllable X-cite mercury lamp and a variety of filter cubes (360, 488, 560, 604 nm excitation) for fluorescence microscopy, as well as a halogen lamp for brightfield and DIC imaging. It also features 4 bright objectives (10, 20, 40, 63x), a high-resolution Hamamatsu Orca R2 CCD camera (1344x1024 pixels) and a motorised stage (XY only). Images were acquired using Leica LAS Extended Annotation software. For the competition binding assay, cells plated in 35 mm glass-bottomed cell culture dishes (Willco Wells) were incubated with GNP@RGD$(GC)_2$-FITC in HBSS buffer for 30 min at 37°C in the presence or absence of 10 mg/mL anti-$\alpha_v\beta_3$ antibody. After washing, peptide binding was assessed by fluorescence microscopy.

Statical Analysis

Data are presented as mean ± SEM of three independent experiments. Dependent variables were analyzed by either pairwise Student's *t*-test or one-way ANOVA, depending on the data analyzed (details are provided in the figure legends), using GraphPad Prism version 9.0.0 (GraphPad Software, San Diego, California USA). $P<0.05$ was considered significant. ***

Results and Discussion

Physicochemical Characterization of Peptide-Functionalised Gold Nanoparticles (b-GNPs)

The UV-vis spectra (Figure 2) of the as-prepared aqueous dispersions of GNPs show a plasmonic band around 520 nm, characteristic of spherical nanoparticles with a 12 nm diameter.[45] This band is sensitive to wavelength shifts, which can be influenced by factors such as particle size, shape, aggregation state, and the surrounding dielectric medium.[46] The spectra from the titration experiments, in which increasing amounts of peptides were gradually added to the GNP dispersion, exhibit similar bathochromic shift trends for both $(GC)_2$ (Figure 2A) and RGD$(GC)_2$ (Figure 2B). However,

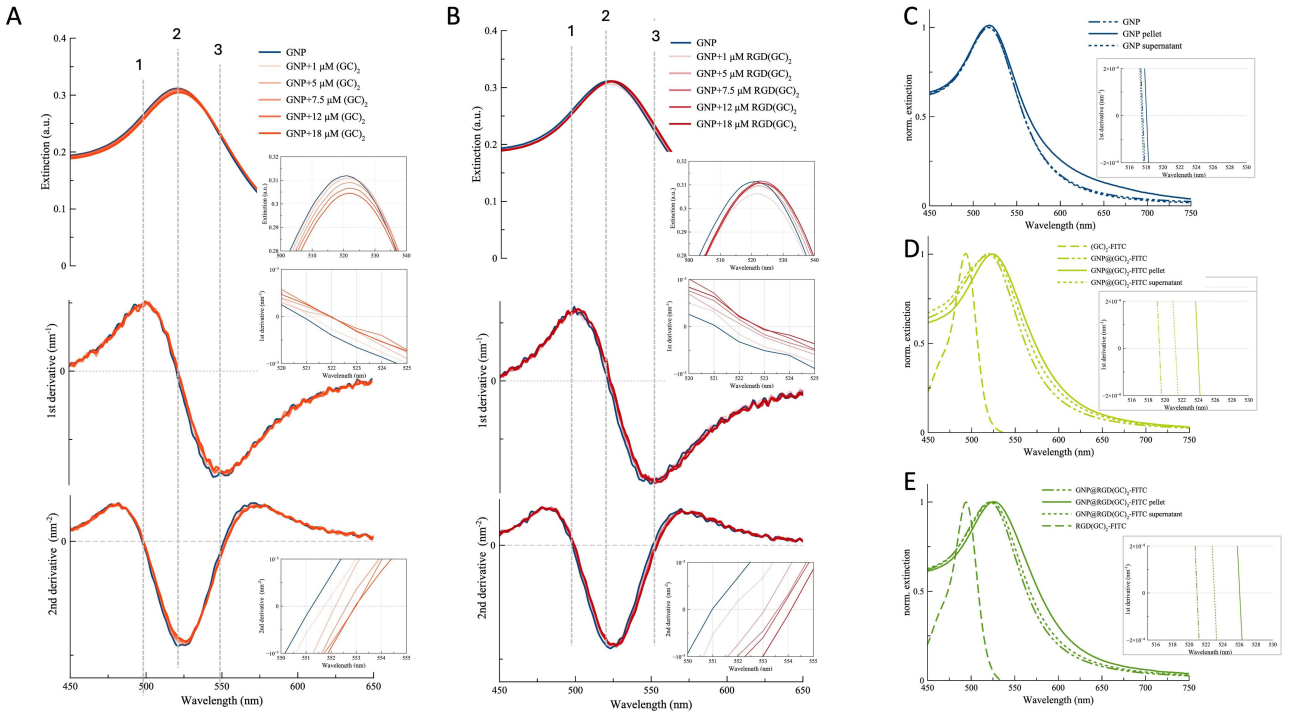

Figure 2 (**A and B**) From top to bottom: extinction, first derivative, and second derivative spectra of 3 nM GNPs (concentration calculated according to equation provided in Materials and Methods) during titration experiments with increasing concentration of $(GC)_2$ (**A**) and RGD$(GC)_2$ (**B**). The dashed lines serve as a guide for the eye, marking the peak maximum (2) and the two inflection points near the maximum in the extinction spectrum (1,3), which correspond to zero-crossing in the first and second order derivative spectra, respectively. (**C–E**) Normalized extinction spectra (insets: magnified view of the second order derivative on the higher wavelength side of the LSPR peak maximum) before and after the centrifugation of: GNP (C), GNP@$(GC)_2$-FITC (D), GNP@RGD$(GC)_2$-FITC (E). The spectra of free $(GC)_2$-FITC and RGD$(GC)_2$-FITC peptides are included as references.

https://doi.org/10.2147/IJN.S527082

$RGD(GC)_2$ demonstrates more pronounced redshifts, as seen at the peak maxima and inflection points. These shifts can be clearly identified by analysing the zero-crossings in the first and second derivative spectra, respectively.[41]

For the fluorescent peptides, a redshift of the plasmon band is still evident, but the most prominent spectral change is the concentration-dependent increase in fluorescence at 488 nm, attributed to FITC (Figure S1). However, after the centrifugation step used to remove unbound or loosely bound peptide molecules, the analysis of UV-vis spectra around the LSPR peak maximum (Figure 2C and D) confirms effective peptide binding, revealing significant differences between the two fluorescent peptides in their adlayers on the GNPs. These differences affect the refractive index at the hybrid biointerface with the metal nanoparticles, resulting in distinct plasmonic shifts. In the pellets, the plasmonic peak is red-shifted by approximately 6 nm for GNP@$(GC)_2$-FITC and 8 nm for GNP@$RGD(GC)_2$-FITC compared to the bare GNPs (see insets of Figure 2C and D).

The results of DLS and ZP analysis are presented in Table 1. Measurements of the dispersions before centrifugation show that the bare GNPs have a hydrodynamic size (d_H) of approximately 20 nm. After centrifugation, the pellets of bare GNPs, resuspended in PBS, show an average particle diameter of about 40 nm. This suggests the formation of dimeric aggregates from individual gold nanoparticles. As expected, the surface charge of the bare gold nanoparticles is negative ($\zeta = -54.5$ mV), which can be attributed to the presence of citrate ions. These ions, used as reducing agents in the synthesis reaction, also function as stabilizers for the colloidal dispersion through an electrostatic repulsion mechanism.[47]

For the peptide-functionalized GNPs, both GNP@$(GC)_2$-FITC and GNP@$RGD(GC)_2$-FITC show no significant changes in particle diameter compared to the bare nanoparticles. This suggests that citrate ions and water molecules in the electric double layer around the core gold nanoparticle have been replaced by peptide molecules without causing a net change in the colloidal hydrodynamic size. In terms of nanoparticle surface charge, the GNPs are negatively charged (with a ζ potential of approximately −50 mV), while the b-GNPs exhibit an almost neutral surface charge. Additionally, a characteristic increase in the polydispersity index (PDI) is observed in the b-GNPs following purification.

Figure 3 shows the morphological characterization by SEM of both bare (GNPs) and peptide-functionalized (b-GNPs) samples. The bare nanoparticles are spherical and monodisperse before centrifugation (Figure 3A), but after centrifugation, dimeric aggregates are clearly visible (Figure 3B). In contrast, the GNP@$(GC)_2$-FITC (Figure 3C) and GNP@$RGD(GC)_2$-FITC (Figure 3D) samples exhibit branched structures, with a higher degree of aggregation observed. Notably, no significant changes are observed on the surface of the GNPs after biofunctionalization (as shown in the magnified insets). Additionally, the changes in nanoparticle size observed from the electron microscopy images are not statistically significant.

Table 1 Zeta Potential (ζ), Hydrodynamic Size (d_H), and Polydispersity Index (PI) Measurements for Bare (GNPs) and Peptide-Functionalized (b-GNPs) Nanoparticles, Both Before and After the Centrifugation Process. The Values Presented are Averages from Three Independent Experiments with Standard Deviation (S.D.)

Sample	ζ (mV)	d_H (nm)	PI
GNPs	−54.5 ± 2.5	20.4 ± 0.5	0.22
GNPs pellet		39 ± 3	0.56
GNP@$(GC)_2$-FITC	−0.2 ± 0.4	19± 2	0.56
GNP@$(GC)_2$-FITC pellet		19± 2	0.77
GNP@$RGD(GC)_2$-FITC	− 2.1 ± 1.5	22 ± 3	0.32
GNP@$RGD(GC)_2$-FITC pellet		20.6 ± 0.9	1.52

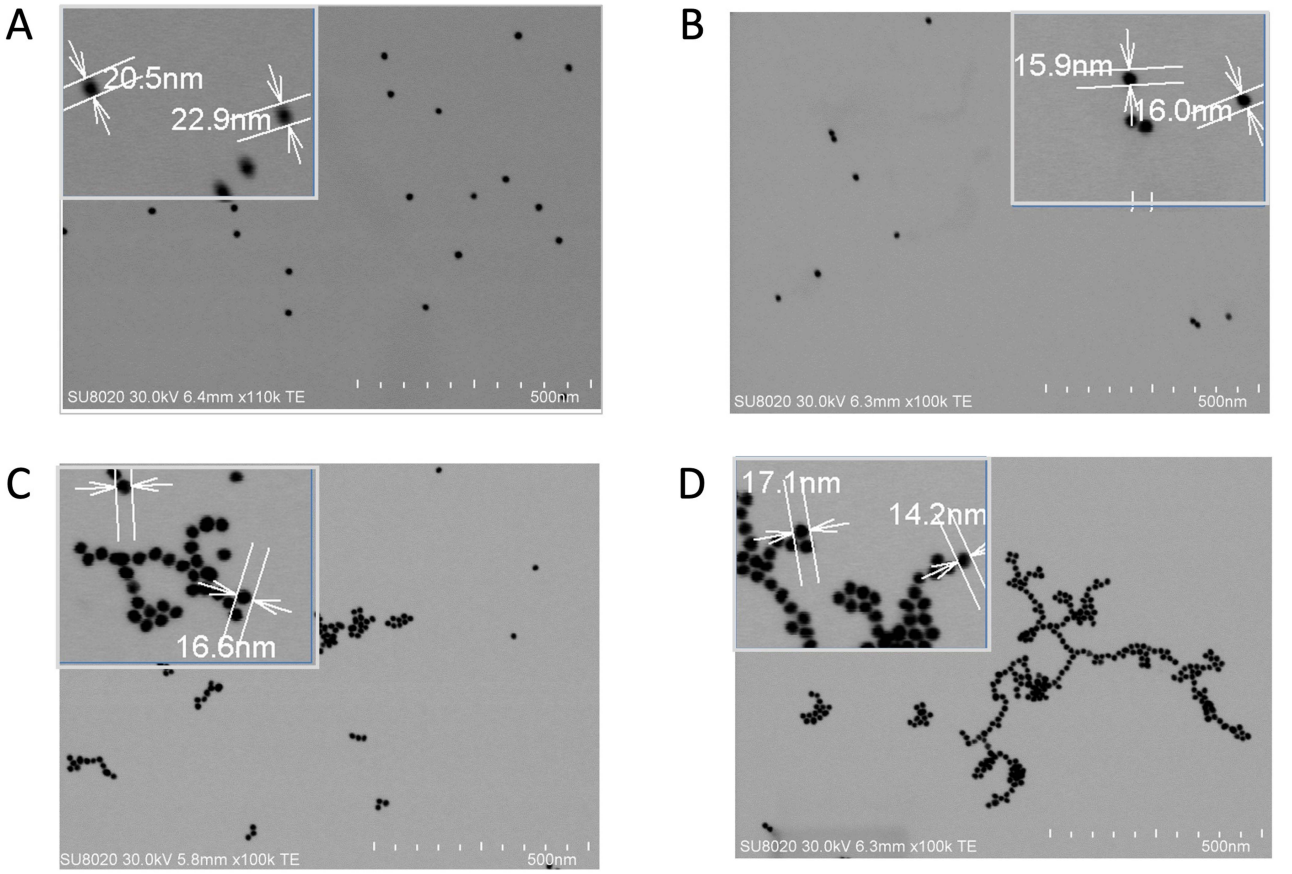

Figure 3 Representative SEM micrographs of GNPs and b-GNPs: bare nanoparticles as prepared (**A**) and after centrifugation (**B**); peptide-functionalized nanoparticles with $(GC)_2$-FITC (**C**) and $RGD(GC)_2$-FITC (**D**).

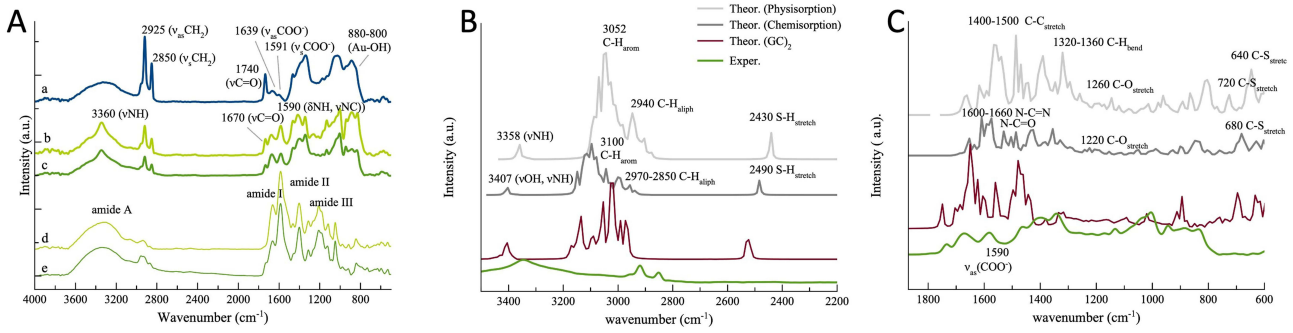

Figure 4 (**A**) Experimental FT-IR spectra of GNPs (line a), GNP@$(GC)_2$-FITC (line b), GNP@$RGD(GC)_2$-FITC (line c), $(GC)_2$-FITC (line d), and $RGD(GC)_2$ (line e). Calculated spectra for physisorption and chemisorption of $RGD(GC)_2$-FITC on GNPs in the comparison with the experimental spectrum of the b-GNP in the high wavenumber range (**B**) and the fingerprint range (**C**) regions. In (**B**) and (**C**) the calculated spectrum for GNP@$(GC)_2$-FITC is included for comparison.

The experimental and calculated FTIR spectra are shown in Figures 4. Figures 4A displays the experimental FTIR spectra for b-GNP samples (lines b and c), compared with reference spectra for bare GNPs (line a) and the peptides alone (lines d and e). The peptide-functionalized nanoparticles, GNP@$(GC)_2$-FITC and GNP@$RGD(GC)_2$-FITC, exhibit characteristic infrared peaks associated with the amide groups: amide I (1600–1800 cm^{-1}), corresponding to the C=O and C=N stretching vibration; amide II (1470–1570 cm^{-1}), corresponding to the N−(C=O)−CH_3 stretch vibration; and amide III (1250–1350 cm^{-1}), attributed to methyl-related C−H or C−C stretch vibrations.[48] Notably, peaks at 1670 cm^{-1}, primarily assigned to C=O stretch vibrations (νC=O), is indicative of β-turns and antiparallel β-sheets in the secondary

https://doi.org/10.2147/IJN.S527082

structure, while a peak at 1590 cm^{-1}, resulting from N-H bending (δNH) and N-C stretching (νNC), further supports the presence of β-structure.[49,50] Additionally, the amide A band, mainly due to the H-N stretch/bend vibration ν(NH) or the hydroxyl H-O-stretch/bend vibration, ν(OH),[48] is also observed. A broad band in the 3300–3500 cm^{-1} range is seen in the free peptides, while the appearance of a ν(NH) peak at 3360 cm^{-1} suggests an ordering effect at the surface of the GNPs, accompanied by the formation of medium strength H-bonds, typical of β-sheet structure.[51,52]

Interestingly, the citrate-related -CH_2- stretching bands at 2925 cm^{-1} ($\nu_{as}CH_2$) and 2850 cm^{-1} (ν_sCH_2)[53] are clearly visible in the GNPs spectrum, as well as the peaks at 1639 cm^{-1} and at 1591 cm^{-1}, assigned to the carboxylate asymmetric stretching ($\nu_{as}COO^-$) bands of citrate molecules strongly adsorbed onto gold nanoparticles and of bulk citrate, respectively.[53] In addition, a peak at 1740 cm^{-1}, ascribed to a non-interacting -COOH (νC=O) onto the GNP surface[54] is also observed. However, these bands are significantly reduced in the b-GNP hybrids, suggesting that the citrate molecules originally attached to the nanoparticle surface, are partially replaced by the peptide molecules. The peaks around 1380 cm^{-1} and 1080 cm^{-1} could correspond to carboxylate symmetric stretching (ν_sCOO^-) and C—O stretching broad bands, respectively.[54,55] On the other hand, a broad band between 880 and 800 cm^{-1}, assigned to vibrations from Au-OH,[56] is clearly visible in GNPs (line a) and, although attenuated, is also present in b-GNP samples.

The comparison between the experimental spectrum of GNP@RGD$(GC)_2$-FITC and the calculated vibrational spectra, shows a closer match between the experimental and calculated spectra for physisorption for the characteristic N-H and O-H stretching bands around 3300 cm^{-1} (Figure 4B). Notably, the S-H stretching band expected between 2430 and 2490 cm^{-1} is absent from the experimental data. This can be likely due to oxidation of the thiol group or due to the fact that this stretching mode of cysteine S-H bonds has a low cross section and the band can be strongly broadened in heterogenous environment.[57] In the fingerprint region, 2000–800 cm^{-1} (Figure 4C), both calculated spectra, for chemisorption and physisorption, closely match the experimental peaks in the absorption bands for amide and guanidine groups between 1580 and 1660 cm^{-1}. In addition, in the calculated spectra, numerous overlapping bands contribute to a broader absorption profile, with R-C-H bending observed between 1320 and 1360 cm^{-1}, C-O stretching around 1220 cm^{-1}, and C-S stretching is seen at 680 cm^{-1}.[58] Additionally, C-H out-of-plane (oop) vibrational modes are observed between 600–900 cm^{-1}. In general, when the peptide is covalently bound to the nanoparticles, the observed frequencies shift slightly to higher values compared to when the peptide is simply physisorbed on the metal surface of the nanoparticle. This suggests that the covalent attachment imposes greater constraints, leading to higher vibrational frequencies.

To note, the main difference in the calculated spectrum for GNP@$(GC)_2$-FITC is a shift of the vibrational modes to higher frequencies, suggesting that the peptide without RGD adopts a more rigid conformation at the surface of GNPs.

XPS analysis (Table 2 and Figure 5) confirms the successful biofunctionalization of GNPs. The C 1s spectra for GNPs (Figure 5A) show components at 284.6 eV (C1), 286.3 eV (C2) and 288.1 eV (C3), which correspond to C-H/C-C, C-O, C=O, respectively. In the spectra of GNP@$(GC)_2$-FITC (Figure 5B) and GNP@RGD$(GC)_2$-FITC (Figure 5C), a new component at 285.9 eV (C4) appears, which is attributed to C-S/C-N.[59] Interestingly, the C2/C4 amplitude ratio is 0.5 for

Table 2 Average Atomic Compositions of Bare GNPs and Hybrid GNP@peptide Samples

Sample	GNPs	GNP@$(GC)_2$-FITC	GNP@RGD$(GC)_2$-FITC
C 1s (at. %)	54.7	52.9	51.4
N 1s (at. %)	-	1.2	1.6
O 1s (at. %)	34.5	43.6	42.5
S 2p (at. %)	-	0.6	0.7
Au 4f (at. %)	10.8	1.7	3.8

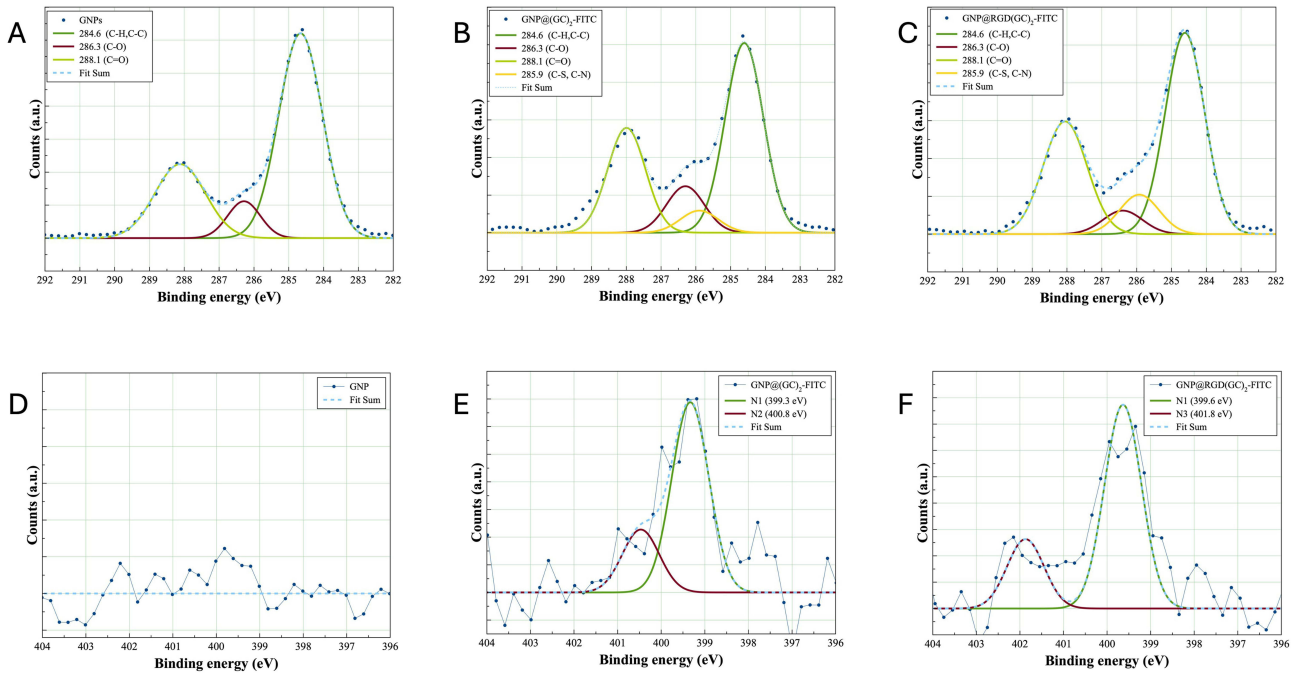

Figure 5 XPS deconvolution analysis of the C 1s (**A-C**) and N 1s (**D-F**) peaks is shown for GNPs (A–D), GNP@$(GC)_2$-FITC (B, E), and GNP@RGD$(GC)_2$-FITC (**C–F**) samples.

GNP@$(GC)_2$-FITC and 1.7 for GNP@RGD$(GC)_2$-FITC, suggesting a greater contribution from C-N bonds in the presence of RGD, as confirmed in the quantitative analysis.

The N 1s XPS peak (Figure 5D and E), though rather noisy, confirms the presence of nitrogen in b-GNPs samples, and also the presence of different oxidation states.[60,61] The tetrapeptide $(GC)_2$ has three N-C=O amide bonds giving photoemission at 399.3±0.2 eV (N1 component), together and a small peak at 400.8±0.2 eV of BE (N2 component) from the amine at the N-terminus in the glycine (Figure 5E). The RGD peptide has two N-C=O amide linkages and a protonated arginine α-NH_3^+ at the N-terminus, resulting in photoemission at 401.8±0.2 eV (N3 component) (Figure 5F). Additional contributions to N1 and N3 components arise from the guanidine group of arginine and protonation by Brønsted donation from aspartic acid's second carboxyl group.[60,61]

XPS analysis of the Au4f 1s and S 2p spectra (Figure S3) further confirms the peptide functionalisation of the GNPs, revealing different adsorption states for the two peptides. A downward shift of 0.2 eV for both GNP@$(GC)_2$-FITC and GNP@RGD$(GC)_2$-FITC (Figure S3B and C) compared to the Au $4f_{5/2}$ (86.4 eV) and Au $4f_{7/2}$ (82.7 eV) doublet[62] in bare GNPs (Figure S3A) suggests interaction, likely charge-transfer effects, between the gold core electrons and peptides.[63]

In the S 2p core level region (Figure S3D–F), the three doublets (2p3/2 and 2p1/2) for the GNP@$(GC)_2$-FITC sample show the main components at 161.1±0.2 eV (S1), 163.4±0.2 eV (S2) and 167.4±0.2 eV (S3), which are attributed to Cys moieties chemisorbed onto gold through thiolate formation,[64,65] sulphur-containing groups not directly bound to gold, and oxidised S atoms,[66] respectively. For GNP@RGD$(GC)_2$-FITC, the S2 component shifts to 164.8±0.2 eV, indicating adsorbed states with slightly different bonding configurations or absorption sites.

The Receptor-Dependent Interaction of b-GNPs with Melanoma WM266 and HeLa Cells

In the cellular experiments, two cell lines were chosen: WM266 (high $\alpha_v\beta_3$ expression) and HeLa (very low or no $\alpha_v\beta_3$ expression). To validate the appropriate cell line for our studies, we first assessed the expression levels of $\alpha_v\beta_3$ integrin on the membrane surface of both WM266 and HeLa cell lines using flow cytometry. The cells were fixed and immunostained with an AlexaFluor488-conjugated anti-integrin $\alpha_v\beta_3$ antibody, as described in the Materials and Methods section. Consistent with previous findings,[67] the histogram in Figure 6 shows that WM266 cells exhibit higher $\alpha_v\beta_3$ expression

https://doi.org/10.2147/IJN.S527082

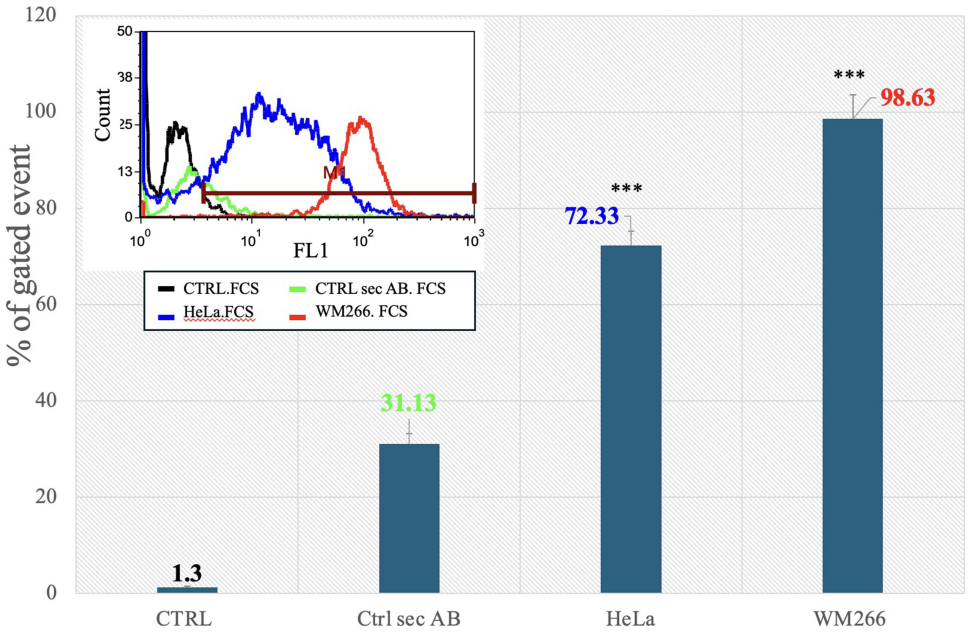

Figure 6 Flow cytometry analysis of $\alpha_v\beta_3$ integrin expression by immunofluorescence in HeLa and WM266 cells. Percentage of gated cells and cytofluorimetric plot (inset) in each population: control (CTRL), control with secondary antibody (Ctrl sec AB), HeLa, and WM266. The gate represents the threshold for positive fluorescence, established based on the negative control incubated with only the AlexaFluor488-conjugated antibody. Statistical analysis was performed by one-way ANOVA with $P<0.05$ was considered significant. *** in HeLa vs Ctrl, and WM266 vs Hela and WM266 vs Ctrl.

compared to HeLa cells. This is further confirmed by the clear separation of the two populations in the cytofluorimetric plots (see inset), signifying a higher concentration of $\alpha_v\beta_3$ molecules in WM266 cells, displaying brighter fluorescence compared to the other cell types and conditions.

The internalisation of GNP@peptide into WM266 cells was examined using epifluorescence microscopy by detecting the FITC signal (Figure 7). Both WM266 and HeLa cells were incubated for 30 minutes at 37°C with 1.6 nM GNP@peptide samples, and the distribution of FITC fluorescence was observed. DAPI staining was used to visualize the cell nuclei. The green fluorescence likely represents nanoparticle aggregates, as likely due to the high ionic strength of the saline aqueous solution in the cellular environment. As shown in Figure 7A, a faint FITC signal was detected in HeLa cells (upper left panel), while in WM266 cells (lower left panel) GNP@RGD(GC)$_2$-FITC displayed diffuse fluorescence throughout the cytosol. In certain instances, the signal was also localized to discrete puncta, consistent with vesicular structures (Figure 7, right panels, yellow circles). These results suggest that, similar to previous findings in U87 glioblastoma cells,[22] in WM266 melanoma cells, expressing high levels of $\alpha_v\beta_3$, the uptake of RGD-functionalised GNPs involves active internalisation via $\alpha_v\beta_3$ integrin-mediated endocytosis. In contrast, HeLa cells, which express lower levels of $\alpha_v\beta_3$ integrin, showed only weak fluorescence, indicating limited nanoparticle uptake.

Under identical experimental conditions, cell treatment with GNP@(GC)$_2$-FITC was used to assess the fluorescence signal resulting from the $\alpha_v\beta_3$-independent uptake of GNPs lacking the RGD motif. The micrographs in Figure S4 show that the presence of RGD motif in the multifunctional cRGD-GCt-FITC capping agent for GNPs results in a strong FITC signal within WM266 cells. In contrast, the absence of RGD, i.e., the treatment with GNP@(GC)$_2$-FITC, resulted in markedly weaker fluorescence in WM266 cells. The observed diffuse and faint signal supports the hypothesis that, in the absence of the RGD sequence, the nanoparticles undergo passive or nonspecific internalization. The lack of punctate staining further implies that endocytosis is not efficiently engaged without $\alpha_v\beta_3$ targeting.

To investigate the mechanism of GNP@RGD(GC)$_2$-FITC uptake, specifically whether it requires a receptor-mediated endocytic pathway, WM266 cells were incubated with or without an anti-$\alpha_v\beta_3$ blocking antibody. The results in Figure 8 show that the blocking the $\alpha_v\beta_3$ receptor with a specific antibody led to a strong reduction in fluorescence following exposure to GNP@RGD(GC)$_2$-FITC (Figure 8B) compared to cells without the anti-$\alpha_v\beta_3$ blocking antibody (Figure 8A), reinforcing the notion that uptake by WM266 cells is dependent on $\alpha_v\beta_3$-mediated

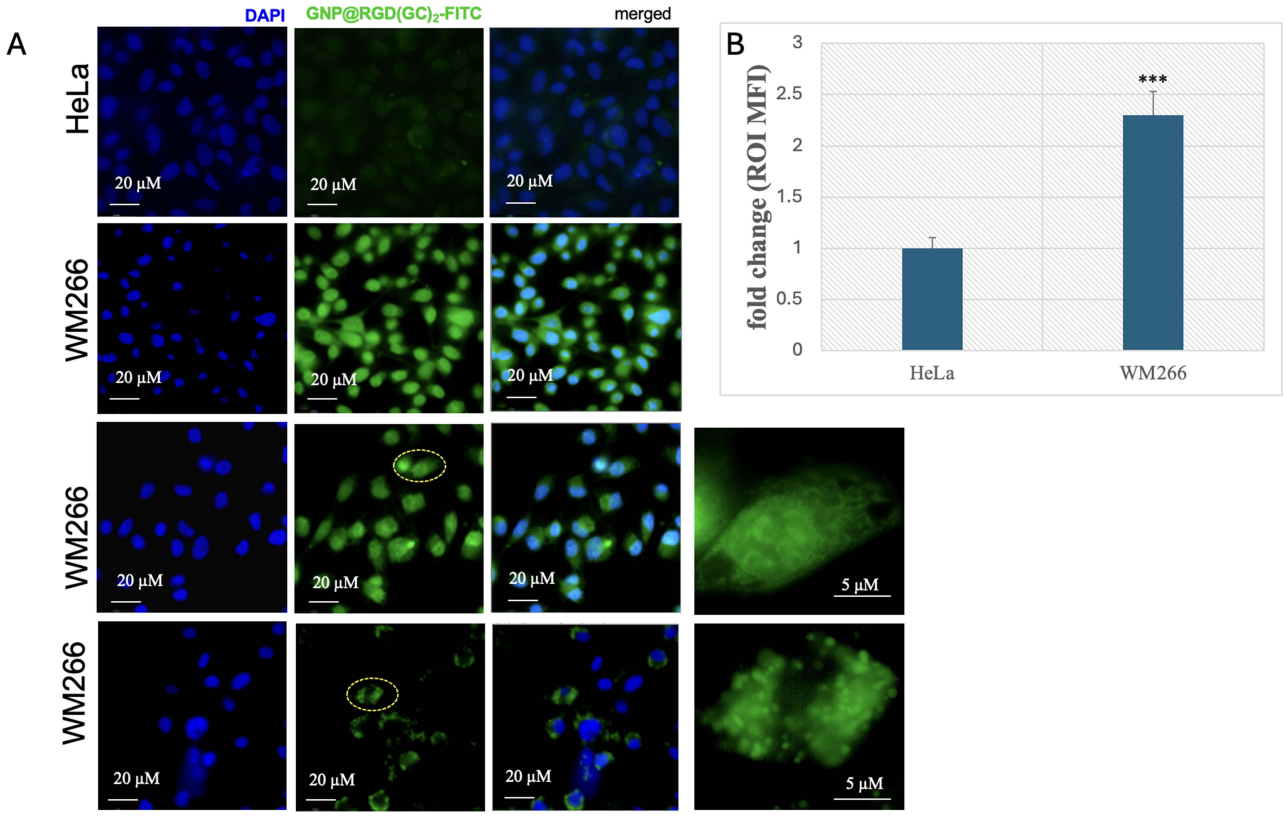

Figure 7 Uptake of GNP@peptides into WM266 and HeLa cells. (**A**) Epifluorescence microscopy images show the distribution of FITC fluorescence in HeLa cells (upper right panels) and WM266 cells (lower right panels) after treatment with the nanoparticles. Panel (**B**) shows histograms quantifying the fold change in the mean fluorescence intensity (MFI) between HeLa and WM266 cells, measured by defining regions of interest (ROI) within each cell and calculating the average fluorescence value after background subtraction. Statistical significance was assessed using a pairwise Student's *t*-test, with *** indicating $p < 0.05$ compared to the control (HeLa).

mechanisms. The residual fluorescence still observed and related to some nanoparticle uptake (Figure 8C) suggests that while $\alpha_v\beta_3$ plays a major role, other non-specific uptake mechanisms may also contribute to internalization.

It is worth mentioning that $\alpha_v\beta_3$ receptor blockade led to noticeable morphological changes in WM266 cells, including cell rounding and increased detachment from the culture surface. These features, related to a disrupted cell adhesion, often precede apoptosis and are consistent with the well-established role of this integrin in promoting cell viability, migration, and angiogenesis.[68]

Discussion

We exploited the plasmonic, vibrational, and chemical properties of GNPs to characterize the nanoparticle surface and conduct in-situ investigations into the formation of the hybrid nano-bio-interface of b-GNP nanocomposites. The insets of Figure 2A and B emphasize the subtle variations in the LSPR signal between $(GC)_2$ and $RGD(GC)_2$, with maximum shifts of approximately 1 nm and 2 nm (at the peak maxima) and around 2 nm and 3 nm (at the inflection points), relative to the original wavelengths of 521 nm and 551 nm of the pristine GNP. This effect is attributed to local changes in the dielectric permittivity following the chemisorption of the peptide onto the gold nanoparticle surface.[69] It should be noted that arginine is positively charged at pH=7.4, as the pKa of the guanidinium group is around 11. Therefore, the greater shift observed for the RGD-containing peptide, which is expected to be positively charged under these experimental conditions, compared to the simple $(GC)_2$ peptide, can be explained by additional electrostatic interactions between the peptide and the metal surface, alongside the covalent thiol bonding.[70]

Moreover, the increase of PDI in b-GNPs following centrifugation indicates significant broad size distribution, which may lead to inconsistent biological responses, particularly in the context of intravenous administration. Larger particles are more likely to be sequestered by the mononuclear phagocyte system, potentially reducing the systemic circulation

https://doi.org/10.2147/IJN.S527082

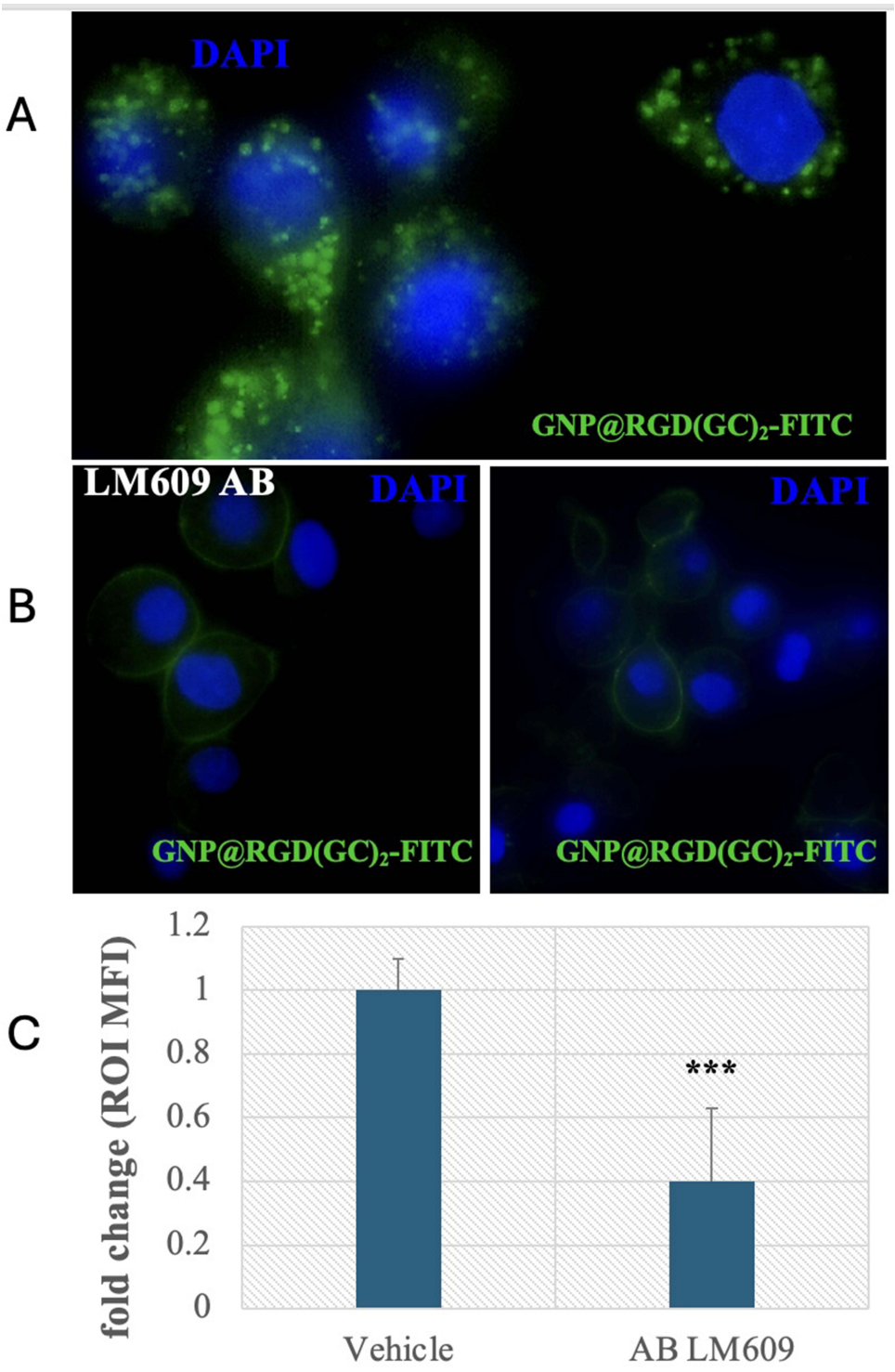

Figure 8 Representative micrographs of WM266 cells treated with GNP@RGD(GC)$_2$-FITC in the absence (**A**) of the presence (**B**) of the anti-$\alpha_v\beta_3$ blocking antibody. Panel (**C**) shows histograms quantifying the fold change in ROI MFI, quantifying the fluorescence intensities observed in panels A and B. Statistical significance was assessed using a pairwise Student's *t*-test, with * * * indicating $p<0.05$ compared to control (vehicle).

time, whereas smaller particles may exhibit enhanced tissue penetration, thereby influencing both the efficacy and safety profile of the formulation.[71] Despite this heterogeneity, the mean diameter of b-GNPs remains largely unchanged in samples measured after centrifugation, suggesting that effective steric stabilisation is provided by the peptide coating and

strong peptide-gold interactions. This stabilisation appears to compensate for the lack of electrostatic repulsion typically offered by citrate, which is absent due to the neutral surface charge of the b-GNPs.

Further evidence for the stability of the b-GNPs is provided by the UV-vis spectra obtained from the flocculation assay (Figure S2). Consistent with the DLS and ζ-potential analyses, the SEM results (Figure 3) confirmed that partial nanoparticle aggregation occurs due to the centrifugation process, as well as coalescence after the drying and exposure to vacuum conditions during microscope analysis. However, these effects are not attributed to intermolecular forces among the peptide molecules coating the b-GNPs, which remain stable.

The FTIR analysis shows clear differences between the peptide functionalised GNPs (b-GNPs) and the bare GNPs (Figure 4). The presence of amide I, II and III bands in the spectra of the b-GNPs is characteristic of the peptide coating and indicates a successful functionalisation of the nanoparticles. The observation of β-turns and antiparallel β-sheets, indicated by peaks at 1670 cm^{-1} and 1590 cm-^{1}, further confirms the secondary structure of the peptide on the surface of the GNPs. In addition, the ordering effect observed in the appearance of the ν(NH) peak at 3360 cm^{-1} suggests that the peptide adopts a structured conformation upon binding to the GNP surface, probably stabilised by hydrogen bonding, typical of β-sheet structures. The significant reduction of citrate-related peaks in the b-GNP spectra suggests that the peptide molecules partially replace the citrate molecules initially adsorbed on the GNPs, which affects the surface chemistry and stability of the nanoparticle. The absence of the expected S-H stretching band in the experimental data for GNP@RGD$(GC)_2$-FITC can be attributed to the oxidation of the thiol group or to the fact that the S-H stretch has a low intensity and is broad in a heterogeneous environment.

The calculated IR spectra for both physisorbed and chemisorbed peptides are in good agreement with the experimental data, with the difference in vibrational frequencies suggesting that covalent attachment of the peptide leads to a more rigid conformation on the GNP surface, as clearly observed for GNP@$(GC)_2$-FITC. The observed shifts to higher frequencies for the covalently bound peptide can be attributed to the constraints imposed by the chemical bond affecting the vibrational modes of the peptide.

The XPS analysis (Figure 5 and Table 2) provides strong evidence for the successful functionalisation of GNPs with peptides and detailed information about the peptide attachment, the interaction between the peptides and the gold surface, and the structural differences between the two peptides. In the N1s peak, the evidence of additional contributions from the guanidine group and protonation of the RGD peptide emphasises the diverse nature of peptide interactions at the nanoparticle surface. The observed 0.2 eV downward shift of the Au4f peaks for b-GNPs suggests charge transfer interactions between the peptide and the gold core. This indicates that the peptides are not simply physisorbed but are likely to form covalent or strong ionic bonds with the gold surface. Analysis of the S 2p peaks, with the shift in the S2 component for the GNP@RGD$(GC)_2$-FITC sample further suggests that the RGD peptide adopts a slightly different configuration compared to the $(GC)_2$ peptide, reflecting variations in the peptide's binding environment and absorption sites on the GNP surface.

The differential expression of $\alpha_v\beta_3$ integrin between HeLa and WM266 cells allowed us to assess the receptor specific uptake of GNP@peptide conjugates. The pronounced internalisation observed in WM266 cells compared to HeLa supports the hypothesis that $\alpha_v\beta_3$ integrin plays a key role in mediating cellular uptake of RGD-functionalised nanoparticles. Importantly, the reduced uptake observed with GNPs lacking the RGD motif confirms that the RGD-$\alpha_v\beta_3$ interaction is critical for efficient nanoparticle internalisation. The remaining low levels of uptake are likely to reflect non-specific pathways that appear insufficient to compensate for the lack of receptor targeting.

Blocking experiments further supported the receptor-mediated mechanism, as pre-treatment with an anti-$\alpha_v\beta_3$ antibody significantly impaired nanoparticle uptake in WM266 cells. Although a modest residual signal of fluorescence was detected, this is consistent with the possibility of alternative, non-receptor-mediated entry routes making a limited contribution.

The morphological changes observed following $\alpha_v\beta_3$ receptor blockade, namely cell rounding and detachment, highlight the critical role of this integrin in maintaining melanoma cell adhesion and cytoskeletal integrity and are consistent with the established function of $\alpha_v\beta_3$ in mediating cell-extracellular matrix interactions that are essential for tumour cell migration, survival and metastasis.[72] For instance, increased cell detachment may reflect a loss of anchorage-dependent survival signals, potentially triggering anoikis, a form of detachment-induced apoptosis.[73] This observation

adds a therapeutic dimension to the use of RGD-functionalised GNPs: in addition to enhancing targeted uptake, these nanoparticles may also sensitise tumour cells to detachment-induced cell death by competitively inhibiting integrin binding. Taken together, these findings demonstrate that GNP@RGD$(GC)_2$ engages $\alpha_v\beta_3$ integrins to facilitate selective and efficient internalisation in melanoma cells, while also disrupting integrin function, a dual effect that may enhance its utility as a complementary anti-cancer strategy. This dual functionality positions these hybrid nanoplatforms as valuable candidates for melanoma theranostics,[74] leveraging also the strong plasmonic properties of gold nanoparticles to enable signal amplification in imaging modalities such as surface-enhanced Raman scattering and photoacoustic imaging.

Conclusion

We have developed and characterised spherical gold nanoparticles (GNPs) biofunctionalised with a multifunctional ligand, cRGD-GCt-FITC, incorporating a cyclic $\alpha_v\beta_3$ integrin-binding RGD motif, a gold-binding glycine-cysteine tetrapeptide and a fluorescein isothiocyanate (FITC) dye. The nanoparticles were synthesised by a simple spontaneous adsorption method and a comprehensive physicochemical characterisation confirmed the successful surface modification. Different binding behaviours between RGD-containing and RGD-free peptides were observed. While the stable mean particle diameter after centrifugation indicates effective steric stabilisation by strong peptide anchoring (despite the loss of electrostatic repulsion), the increased polydispersity index reflects size heterogeneity, which could affect biological performance. Future optimisation will therefore focus on refining the size distribution of the nanoparticles through improved synthesis or fractionation techniques to improve their consistency for biomedical use.

Biological evaluation in $\alpha_v\beta_3$-overexpressing WM266 melanoma cells revealed that RGD-functionalised GNPs undergo receptor-mediated endocytosis, supporting their specificity for integrin-targeted delivery. Furthermore, cell rounding and detachment following integrin blockade highlight the functional importance of $\alpha_v\beta_3$ in maintaining cell adhesion and morphology, with potential implications for therapeutic disruption of tumour cell viability.

While our findings support the potential of these biomimetic nanoparticles for targeted delivery and integrin-interfering cancer therapy, further investigation is required to evaluate their cytotoxic, anti-angiogenic or anti-metastatic effects. Further studies are planned to assess the biocompatibility, safety profile, and therapeutic efficacy of these nanoparticles in both malignant and non-malignant cellular models. Future work will also explore their diagnostic potential, exploiting the plasmonic properties of gold for imaging modalities. These efforts will help to establish the dual therapeutic and diagnostic (theranostic) capabilities of this platform in preclinical cancer models, advancing its development towards targeted and image-guided cancer treatment.

Acknowledgments

The authors gratefully acknowledge Yoann Paint (Materia Nova, Mons) for the technical assistance on the SEM measurements, Giorgio Varriale and Massimiliano Mazzucchi (IBB, Naples) for IT assistance.

Funding

The authors declare that financial support was received for the research, authorship, and/or publication of this article. This work has been partially funded by the European Union (Next Generation EU), through the MUR (Ministero dell'Università e della Ricerca)-PNRR project SAMOTHRACE (ECS00000022). Moreover, the financial support by the MUR in the framework of the PRIN2022-PNRR call under project CoMu4CaT is acknowledged.

Disclosure

The authors report no conflicts of interest in this work.

References

1. Hu X, Zhang Y, Ding T, Liu J, Zhao H. Multifunctional gold nanoparticles: a novel nanomaterial for various medical applications and biological activities. *Front Bioeng Biotechnol*. 2020;8. doi:10.3389/fbioe.2020.00990.
2. Wang W, Wang J, Ding Y. Gold nanoparticle-conjugated nanomedicine: design, construction, and structure–efficacy relationship studies. *J Mat Chem B*. 2020;8(22):4813–4830. doi:10.1039/c9tb02924a

3. Arcos Rosero WA, Bueno BA, Daruich de Souza C, Chuery Martins Rostelato ME. Review of advances in coating and functionalization of gold nanoparticles: from theory to biomedical application. *Pharmaceutics*. 2024;16(2). doi:10.3390/pharmaceutics16020255
4. Cucci LM, Trapani G, Ö H, La Mendola D, Satriano C. Gold nanoparticles functionalized with angiogenin for wound care application. *Nanomaterials*. 2021;11(1):201. doi:10.3390/nano11010201
5. Di Pietro P, Caporarello N, Anfuso CD, et al. Immobilization of neurotrophin peptides on gold nanoparticles by direct and lipid-mediated interaction: a new multipotential therapeutic nanoplatform for CNS disorders. *ACS Omega*. 2017;2(8):4071–4079. doi:10.1021/acsomega.7b00458
6. Di Pietro P, Strano G, Zuccarello L, Satriano C. Gold and silver nanoparticles for applications in theranostics. *Curr. Top. Med. Chem*. 2016;16 (27):3069–3102. doi:10.2174/1568026616666160715163346
7. Zhang Q, Hou D, Wen X, et al. Gold nanomaterials for oral cancer diagnosis and therapy: advances, challenges, and prospects. *Mater Today Bio*. 2022;15:100333. doi:10.1016/j.mtbio.2022.100333
8. Yasin D, Sami N, Afzal B, et al. Prospects in the use of gold nanoparticles as cancer theranostics and targeted drug delivery agents. *Appl. Nanosci*. 2022;13(6):4361–4393. doi:10.1007/s13204-022-02701-5
9. Jha A, Kumar M, Mishra B. Gold nanoparticles as theranostic platform. *Inorganic Nanosystems*. 2023;279–321.
10. Zamborlin A, Voliani V. Gold nanoparticles as antiangiogenic and antimetastatic agents. *Drug Discov. Today*. 2023;28(2):103438. doi:10.1016/j.drudis.2022.103438
11. Amina SJ, Guo B. A review on the synthesis and functionalization of gold nanoparticles as a drug delivery vehicle. *Int J Nanomed*. 2020;15:9823–9857. doi:10.2147/ijn.S279094
12. Tan KF, In LLA, Vijayaraj Kumar P. Surface functionalization of gold nanoparticles for targeting the tumor microenvironment to improve antitumor efficiency. *ACS Appl. Bio Mater*. 2023;6(8):2944–2981. doi:10.1021/acsabm.3c00202
13. Foti A, Clépoint B, Fraix A, D'Urso L, De Bonis A, Satriano C. A simple approach for CTAB-free and biofunctionalized gold nanorods to construct photothermal active nanomedicine for potential in vivo applications in cancer cells and scar treatment. *Front Mater*. 2024;11. doi:10.3389/fmats.2024.1381176.
14. Bugatti K, Sartori A, Battistini L, et al. Nintedanib-αVβ3 integrin ligand dual-targeting conjugates towards precision treatment of melanoma. *Eur. J. Org. Chem*. 2022;2022(45). doi:10.1002/ejoc.202200765
15. Zhang L, Meng X, Shan X, et al. Integrin αvβ3-specific hydrocyanine for cooperative targeting of glioblastoma with high sensitivity and specificity. *Anal. Chem*. 2019;91(19):12587–12595. doi:10.1021/acs.analchem.9b03725
16. Hsin IL, Chiu L-Y, Ko JL, Wang P-H, Wu PJ. Targeted inhibition of integrin αVβ3 induces cytotoxicity and suppresses migration ability in ovarian cancer cells and tumor spheroids. *Int J Med Sci*. 2025;22(7):1544–1554. doi:10.7150/ijms.103141
17. Desgrosellier JS, Cheresh DA. Integrins in cancer: biological implications and therapeutic opportunities. *Nat Rev Cancer*. 2010;10(1):9–22. doi:10.1038/nrc2748
18. Mezu-Ndubuisi OJ, Maheshwari A. The role of integrins in inflammation and angiogenesis. *Pediatr Res*. 2020;89(7):1619–1626. doi:10.1038/s41390-020-01177-9
19. Serini G, Valdembri D, Bussolino F. Integrins and angiogenesis: a sticky business. *Exp. Cell. Res*. 2006;312(5):651–658. doi:10.1016/j.yexcr.2005.10.020
20. Gu Y, Dong B, He X, et al. The challenges and opportunities of αvβ3-based therapeutics in cancer: from bench to clinical trials. *Pharmacol Res*. 2023;189:106694. doi:10.1016/j.phrs.2023.106694
21. Yin H-Q, Mai D-S, Gan F, Chen X-J. One-step synthesis of linear and cyclic RGD conjugated gold nanoparticles for tumour targeting and imaging. *RSC Adv*. 2014;4(18):9078. doi:10.1039/c3ra47729k
22. Scarì G, Porta F, Fascio U, et al. Gold nanoparticles capped by a GC-containing peptide functionalized with an rgd motif for integrin targeting. *Bioconjugate Chem*. 2012;23(3):340–349. doi:10.1021/bc200143d
23. Arosio D, Manzoni L, Araldi EMV, Scolastico C. Cyclic RGD functionalized gold nanoparticles for tumor targeting. *Bioconjugate Chem*. 2011;22 (4):664–672. doi:10.1021/bc100448r
24. Liang G, Jin X, Zhang S, Xing D. RGD peptide-modified fluorescent gold nanoclusters as highly efficient tumor-targeted radiotherapy sensitizers. *Biomaterials*. 2017;144:95–104. doi:10.1016/j.biomaterials.2017.08.017
25. Biscaglia F, Ripani G, Rajendran S, et al. Gold nanoparticle aggregates functionalized with cyclic rgd peptides for targeting and imaging of colorectal cancer cells. *ACS Appl. Nano Mater*. 2019;2(10):6436–6444. doi:10.1021/acsanm.9b01392
26. Kim YH, Jeon J, Hong SH, et al. Tumor targeting and imaging using cyclic RGD-pegylated gold nanoparticle probes with directly conjugated iodine-125. *Small*. 2011;7(14):2052–2060. doi:10.1002/smll.201100927
27. Perrins RD, McCarthy L-A, Robinson A, et al. Targeting ultrasmall gold nanoparticles with cRGD peptide increases the uptake and efficacy of cytotoxic payload. *Nanomaterials*. 2022;12(22):4013. doi:10.3390/nano12224013
28. Maggi V, Bianchini F, Portioli E, et al. Gold nanoparticles functionalized with rgd-semipeptides: a simple yet highly effective targeting system for αVβ3 integrins. *Chem Eur J*. 2018;24(46):12093–12100. doi:10.1002/chem.201801823
29. Yin H-Q, Bi F-L, Gan F. Rapid synthesis of cyclic RGD conjugated gold nanoclusters for targeting and fluorescence imaging of melanoma A375 cells. *Bioconjugate Chem*. 2015;26(2):243–249. doi:10.1021/bc500505c
30. Javed R, Khan B, Sharafat U, et al. Dynamic interplay of metal and metal oxide nanoparticles with plants: influencing factors, action mechanisms, and assessment of stimulatory and inhibitory effects. *Ecotoxicol Environ Saf*. 2024;271:115992. doi:10.1016/j.ecoenv.2024.115992
31. Hosseinikhah SM, Vahdat-Lasemi F, Farhoudi L, Gupta G, Kesharwani P, Sahebkar A. RGD-decorated nanoparticles: therapeutic potential beyond cancer. *J Drug Delivery Sci Technol*. 2024;98:105924. doi:10.1016/j.jddst.2024.105924
32. Zhang R, Kiessling F, Lammers T, Pallares RM. Clinical translation of gold nanoparticles. *Drug Delivery Transl Res*. 2022;13(2):378–385. doi:10.1007/s13346-022-01232-4
33. He Z, Liu J, Du L. The unexpected effect of PEGylated gold nanoparticles on the primary function of erythrocytes. *Nanoscale*. 2014;6 (15):9017–9024. doi:10.1039/c4nr01857e
34. Shi D, Beasock D, Fessler A, et al. To PEGylate or not to PEGylate: immunological properties of nanomedicine's most popular component, polyethylene glycol and its alternatives. *Adv. Drug Delivery Rev*. 2022;180. doi:10.1016/j.addr.2021.114079
35. Huang YC, Yang YC, Yang KC, et al. Pegylated gold nanoparticles induce apoptosis in human chronic myeloid leukemia cells. *Biomed Res. Int*. 2014;2014:1–9. doi:10.1155/2014/182353

36. Depalo N, Corricelli M, De Paola I, et al. NIR emitting nanoprobes based on cyclic RGD motif conjugated pbs quantum dots for integrin-targeted optical bioimaging. *ACS Appl. Mater. Interfaces*. 2017;9(49):43113–43126. doi:10.1021/acsami.7b14155
37. Di Pietro P, Zaccaro L, Comegna D, et al. Silver nanoparticles functionalized with a fluorescent cyclic RGD peptide: a versatile integrin targeting platform for cells and bacteria. *RSC Adv.* 2016;6(113):112381–112392. doi:10.1039/c6ra21568h
38. Ditta SA, Yaqub A, Tanvir F, et al. Gold nanoparticles capped with L-glycine, L-cystine, and L-tyrosine: toxicity profiling and antioxidant potential. *J Mater Sci*. 2023;58(6):2814–2837. doi:10.1007/s10853-023-08209-9
39. Krpetić Ž, Nativo P, Porta F, Brust M. A multidentate peptide for stabilization and facile bioconjugation of gold nanoparticles. *Bioconjugate Chem*. 2009;20(3):619–624. doi:10.1021/bc8003028
40. Liu X, Atwater M, Wang J, Huo Q. Extinction coefficient of gold nanoparticles with different sizes and different capping ligands. *Colloids Surf. B*. 2007;58(1):3–7. doi:10.1016/j.colsurfb.2006.08.005
41. Chen P, Tran NT, Wen X, Xiong Q, Liedberg B. Inflection point of the localized surface plasmon resonance peak: a general method to improve the sensitivity. *ACS Sens*. 2017;2(2):235–242. doi:10.1021/acssensors.6b00633
42. Zhao Y, Truhlar DG. A new local density functional for main-group thermochemistry, transition metal bonding, thermochemical kinetics, and noncovalent interactions. *J. Chem. Phys*. 2006;125(19). doi:10.1063/1.2370993
43. Stewart JJP. Optimization of parameters for semiempirical methods V: modification of NDDO approximations and application to 70 elements. *J. Mol. Model*. 2007;13(12):1173–1213. doi:10.1007/s00894-007-0233-4
44. Tomasella P, Sanfilippo V, Bonaccorso C, et al. Theranostic nanoplatforms of thiolated reduced graphene oxide nanosheets and gold nanoparticles. *Appl Sci*. 2020;10(16):5529. doi:10.3390/app10165529
45. Burda C, Chen X, Narayanan R, El-Sayed MA. Chemistry and properties of nanocrystals of different shapes. *Chem. Rev.* 2005;105(4):1025–1102. doi:10.1021/cr030063a
46. Kreibig U, Genzel L. Optical absorption of small metallic particles. *Surf Sci*. 1985;156:678–700. doi:10.1016/0039-6028(85)90239-0
47. Brewer SH, Glomm WR, Johnson MC, Knag MK, Franzen S. Probing BSA binding to citrate-coated gold nanoparticles and surfaces. *Langmuir*. 2005;21(20):9303–9307. doi:10.1021/la050588t
48. Ji Y, Yang X, Ji Z, et al. DFT-Calculated IR Spectrum Amide I, II, and III Band Contributions of N-Methylacetamide Fine Components. *ACS Omega*. 2020;5(15):8572–8578. doi:10.1021/acsomega.9b04421
49. Zhao J, Ruan Y, Zheng Z, et al. Gold nanoparticles-anchored peptides enable precise colorimetric estimation of microplastics. *Iscience*. 2023;26(6). doi:10.1016/j.isci.2023.106823
50. Hauptmann A, Hoelzl G, Mueller M, Bechtold-Peters K, Loerting T. Raman marker bands for secondary structure changes of frozen therapeutic monoclonal antibody formulations during thawing. *J Pharmaceut Sci*. 2023;112(1):51–60. doi:10.1016/j.xphs.2022.10.015
51. Egorova EA, van Rijt MMJ, Sommerdijk N, et al. One peptide for them all: gold nanoparticles of different sizes are stabilized by a common peptide amphiphile. *ACS Nano*. 2020;14(5):5874–5886. doi:10.1021/acsnano.0c01021
52. Porta F, Speranza G, Ž K, Dal Santo V, Francescato P, Scarì G. Gold nanoparticles capped by peptides. *"Mater. Eng. Res*. 2007;140(3):187–194. doi:10.1016/j.mseb.2007.03.019
53. Wulandari P, Li X, Tamada K, Hara M. Conformational study of citrates adsorbed on gold nanoparticles using Fourier transform infrared spectroscopy. *J Nonlinear Opt Phys Mater*. 2012;17(02):185–192. doi:10.1142/s0218863508004032
54. Sakellari GI, Hondow N, Gardiner PHE. Factors Influencing the surface functionalization of citrate stabilized gold nanoparticles with cysteamine, 3-mercaptopropionic acid or l-selenocystine for sensor applications. *Chemosensors*. 2020;8(3):80. doi:10.3390/chemosensors8030080
55. Segneanu A-E, Vlase G, Lukinich-Gruia AT, Herea DD, Grozescu I. Untargeted metabolomic approach of Curcuma longa to neurodegenerative phytocarrier system based on silver nanoparticles. *Antioxidants*. 2022;11(11):2261. doi:10.3390/antiox11112261
56. Dickson J, Weaver B, Vivekanand P, Basu S. Anti-neoplastic effects of gold nanoparticles synthesized using green sources on cervical and melanoma cancer cell lines. *BioNanoScience*. 2023;13(1):194–202. doi:10.1007/s12668-022-01056-z
57. Deniz E, Schmidt-Engler JM, Ulrich K, Oberle M, Wille G, Bredenbeck J. SH—It happens: s–H bonds as intrinsic 2D-IR labels in proteins. *J. Chem. Phys*. 2022;157(13). doi:10.1063/5.0107057
58. Ferrari P, Berden G, Redlich B, Waters LB, Bakker JM. Laboratory infrared spectra and fragmentation chemistry of sulfur allotropes. *Nat Commun*. 2024;15(1). doi:10.1038/s41467-024-50303-2
59. Wang H, Zhou H, Gestos A, et al. Robust, electro-conductive, self-healing superamphiphobic fabric prepared by one-step vapour-phase polymerisation of poly(3,4-ethylenedioxythiophene) in the presence of fluorinated decyl polyhedral oligomeric silsesquioxane and fluorinated alkyl silane. *Soft Matter*. 2013;9(1):277–282. doi:10.1039/c2sm26871j
60. Stevens JS, Byard SJ, Schroeder SLM. Characterization of proton transfer in co-crystals by x-ray photoelectron spectroscopy (XPS). *Cryst. Growth Des*. 2010;10(3):1435–1442. doi:10.1021/cg901481q
61. Stevens JS, de Luca AC, Pelendritis M, et al. Quantitative analysis of complex amino acids and RGD peptides by X-ray photoelectron spectroscopy (XPS). *Surf Interface Anal*. 2013;45(8):1238–1246. doi:10.1002/sia.5261
62. Joseph Y, Besnard I, Rosenberger M, et al. Self-assembled gold nanoparticle/alkanedithiol films: preparation, electron microscopy, XPS-analysis, charge transport, and vapor-sensing properties. *J Phys Chem A*. 2003;107(30):7406–7413. doi:10.1021/jp030439o
63. Martí A, Costero AM, Gaviña P, et al. Functionalized gold nanoparticles as an approach to the direct colorimetric detection of DCNP nerve agent simulant. *Eur. J. Org. Chem*. 2013;2013(22):4770–4779. doi:10.1002/ejoc.201300339
64. Semenov A, Spatz JP, Möller M, et al. Controlled arrangement of supramolecular metal coordination arrays on surfaces. *Angew. Chem. Int. Ed*. 1999;38(17):2547–2550. doi:10.1002/(sici)1521-3773(19990903)38:17
65. Zhong C-J, Porter MD. Evidence for carbon-sulfur bond cleavage in spontaneously adsorbed organosulfide-based monolayers at Gold. *J Am Chem Soc*. 2002;116(25):11616–11617. doi:10.1021/ja00104a071
66. Setiawan LD, Baumann H, Gribbin D. Surface studies of keratin fibers and related model compounds using ESCA. I—intermediate oxidation products of the model compound 1-cystine and their hydrolytical behaviour. *Surf Interface Anal*. 2004;7(4):188–195. doi:10.1002/sia.740070406
67. Farina B, de Paola I, Russo L, et al. A Combined NMR and computational approach to determine the RGDechi-hCit-αvβ3 integrin recognition mode in isolated cell membranes. *Chem Eur J*. 2015;22(2):681–693. doi:10.1002/chem.201503126
68. Szekacs I, Farkas E, Gemes BL, Takacs E, Szekacs A, Horvath R. Integrin targeting of glyphosate and its cell adhesion modulation effects on osteoblastic MC3T3-E1 cells revealed by label-free optical biosensing. *Sci Rep*. 2018;8(1). doi:10.1038/s41598-018-36081-0

69. Ryu KR, Kim GW, Ha JW. Localized surface plasmon resonance inflection points for improved detection of chemisorption of 1-alkanethiols under total internal reflection scattering microscopy. *Sci Rep*. 2021;11(1). doi:10.1038/s41598-021-92410-w
70. Parak WJ, Qian W, Murakami M, et al. Stable gold nanocolloids with controllable surface modification and functionalization. *Presented at*. 2012.
71. Takeuchi I, Nobata S, Oiri N, Tomoda K, Makino K. Biodistribution and excretion of colloidal gold nanoparticles after intravenous injection: effects of particle size. *Bio-Med. Mater. Eng*. 2017;28(3):315–323. doi:10.3233/bme-171677
72. Aguzzi MS, Fortugno P, Giampietri C, Ragone G, Capogrossi MC, Facchiano A. Intracellular targets of RGDS peptide in melanoma cells. *Mol Cancer*. 2010;9(1). doi:10.1186/1476-4598-9-84
73. Kim Y-N, Koo KH, Sung JY, Yun U-J, Kim H. anoikis resistance: an essential prerequisite for tumor metastasis. *Int J Cell Biol*. 2012;2012:1–11. doi:10.1155/2012/306879
74. Dastgheib ZS, Abolmaali SS, Farahavar G, Salmanpour M, Tamaddon AM. Gold nanostructures in melanoma: advances in treatment, diagnosis, and theranostic applications. *Heliyon*. 2024;10(15):e35655. doi:10.1016/j.heliyon.2024.e35655